Local-Nonlinearity-Enabled Deep Subdiffraction Control of Acoustic Waves

Jiaxin Zhong,[1,2,*] Chengbo Hu,[1,*] Kangkang Wang,[1] Jun Ji,[2] Tao Zhuang,[1,3] Haishan Zou,[1] Jing Lu,[1,3] Hyeonu Heo,[2] Bin Liang,[1,†] Yun Jing,[2,‡] and Jian-Chun Cheng[1,§]

[1]*Key Laboratory of Modern Acoustics and Institute of Acoustics, Nanjing University, Nanjing 210093, China*
[2]*Graduate Program in Acoustics, The Pennsylvania State University, University Park, Pennsylvania 16802, USA*
[3]*NJU-Horizon Intelligent Audio Lab, Horizon Robotics, Beijing 100094, China*

(Received 13 April 2023; accepted 30 October 2023; published 6 December 2023)

Diffraction sets a natural limit for the spatial resolution of acoustic wave fields, hindering the generation and recording of object details and manipulation of sound at subwavelength scales. We propose to overcome this physical limit by utilizing nonlinear acoustics. Our findings indicate that, contrary to the commonly utilized cumulative nonlinear effect, it is in fact the local nonlinear effect that is crucial in achieving subdiffraction control of acoustic waves. We theoretically and experimentally demonstrate a deep subwavelength spatial resolution up to $\lambda/38$ in the far field at a distance 4.4 times the Rayleigh distance. This Letter represents a new avenue towards deep subdiffraction control of sound, and may have far-reaching impacts on various applications such as acoustic holograms, imaging, communication, and sound zone control.

DOI: 10.1103/PhysRevLett.131.234001

Introduction.—Manipulating wavefronts at subwavelength scales has long posed a challenge due to the limitations imposed by the diffraction limit. For example, in acoustic holograms, the spatial resolution of the target image is restricted to about half of the operating wavelength unless the imaging plane is brought into extremely close proximity to the source—a small fraction of the wavelength, where the evanescent waves are still present [1–6]. This limitation also applies to acoustic imaging, where the diffraction law restricts the ability to resolve subwavelength details of an object [7–9]. Furthermore, the size of the source aperture imposes additional constraints, as energy peaks in sound fields cannot extend beyond the Rayleigh distance, which is determined by both the source aperture size and wavelength [10,11]. Consequently, for a given source aperture size and frequency, it is only possible to generate the desired acoustic fields within a certain distance. Alternatively, to generate the desired acoustic fields at a specific frequency and distance, there exists a minimum source aperture size requirement, which can become quite substantial at low frequencies. Collectively, diffraction hinders precise control of sound fields, particularly in the far field, defined by the Rayleigh distance.

Various metamaterials have been proposed to achieve subwavelength control of waves owing to their exceptional optical or acoustical properties [12–19]. Inspired by Pendry's seminal work on the theory of perfect lens [20], near-field superlenses using surface plasmon excitation have been demonstrated, offering subdiffraction–limited resolution by amplifying evanescent waves [19,21,22]. Far-field superlenses with subwavelength resolution [23–25] have also been demonstrated by separately converting different evanescent wave components into propagating waves. Meanwhile, hyperlenses based on strong anisotropy [9,26–28] have been proposed to convert evanescent waves into propagating waves and transfer subwavelength information to the far field over a broader bandwidth than that of superlens. Other metamaterials that have been used for superresolution imaging include, but are not limited to, double-negative metamaterials [4,6], hyperbolic metamaterials [29], and Fabry-Perot resonance-based metamaterials [30]. Nevertheless, a major limitation of metamaterials for subwavelength manipulation is that they have to be placed in the near field of the source to capture the evanescent wave, which may not always be practical. A variety of other strategies have also been proposed to achieve subdiffraction control of waves, such as superoscillation [31,32], time reversal [33], and deep learning-based imaging [34].

In this Letter, we present a new mechanism based on acoustic nonlinearity for achieving far-field superresolution focusing. Acoustic focusing represents the most basic manifestation of an acoustic hologram, and constitutes the first step in conventional acoustic imaging. Despite the crucial role that nonlinearity plays in various acoustics applications, such as nondestructive testing [35], high-intensity focused ultrasound [36], parametric arrays [37], acoustic levitation [38], and midair haptics [39], it remains largely unexplored as a means to achieve acoustic superresolution focusing. During acoustic wave propagation, two types of nonlinearities typically exist [40,41]. Cumulative nonlinear effects have traditionally been considered the dominant factor in facilitating many nonlinear acoustics applications, such as generating directional

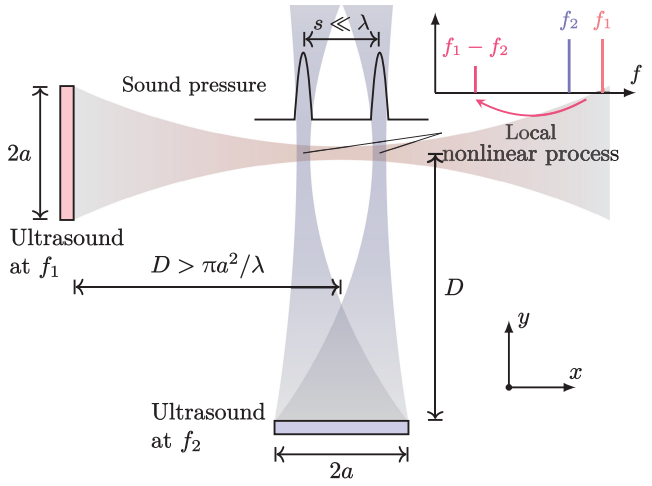

FIG. 1. Illustration of the local-nonlinearity-enabled subdiffraction focusing using two orthogonally placed ultrasound sources operating at frequencies of f_1 and f_2, respectively. The DFW at the frequency of $f = f_1 - f_2$ is nonlinearly generated in the overlapped region, which consists of two focal points. The distance between the ultrasound source and the focal region (D) is greater than the Rayleigh distance for the DFW ($\pi a^2/\lambda$), where λ is the wavelength of the DFW. The spacing between the two focal points (s) is considerably smaller than the wavelength λ at the difference frequency.

low-frequency beams in parametric arrays [37], and producing superharmonics in high-intensity ultrasound imaging [42,43]. Conversely, local nonlinearity, which is determined by the local Lagrangian density of primary waves, is independent of the medium nonlinear coefficient and is frequently overlooked in current nonlinear acoustic applications. This Letter reveals that, while the cumulative nonlinear effect blurs the focusing pattern, the local nonlinear effect holds the key to achieving superresolution acoustics.

Physical model.—The physical model for demonstrating subdiffraction focusing by harnessing local nonlinearity is illustrated in Fig. 1. Two ultrasound line sources are placed on the left and bottom ends of a 2D domain, emitting ultrasound waves with carrier frequencies of f_1 and f_2, respectively, where $f_1 > f_2$. Each source has a length of $2a$. The ultrasound source on the left generates a focused beam with a focal length of D. The ultrasound source on the bottom generates a wave field possessing two focal beams separated horizontally at the focal plane by a distance of s. The focal plane is again at a distance of D away from the source. When both ultrasound waves are driven at high power, e.g., exhibiting a sound pressure level > 130 dB, a difference-frequency wave (DFW) at the frequency of $f = f_1 - f_2$ is nonlinearly generated in the area where the two ultrasound fields intersect, which are two focal points as shown in Fig. 1.

In a homogeneous and viscous fluid such as air, the acoustic wave with finite amplitude is governed by the extended second-order nonlinear wave equation [44], see Sec. 1 of Supplemental Material for details [45]. Under this framework, the sound field of the DFW is composed of two components: (i) the cumulative nonlinear effect, which can be interpreted as the radiation from a virtual source whose source density is proportional to the strength of ultrasound field; and (ii) the local nonlinear effect, which is governed by the local Lagrangian density of the ultrasound. The total sound field at a field point $\mathbf{r}$ is the sum of these two components, which reads

$$p_{\mathrm{tot}}(\mathbf{r}) = p_{\mathrm{cum}}(\mathbf{r}) + p_{\mathrm{loc}}(\mathbf{r}). \tag{1}$$

Under the quasilinear approximation, the cumulative component is the solution of the Helmholtz equation $(\nabla^2 + k^2)p_{\mathrm{cum}} = \beta\omega^2 p_1 p_2^*/(\rho_0 c_0^4)$, where the superscript "*" is the complex conjugation, p_i is the ultrasound pressure at the frequency of f_i, $i = 1, 2$, β is the nonlinearity coefficient, ρ_0 is the air density, and c_0 is the speed of sound of linear acoustics [44,51]. The cumulative component of the DFW sound field can be obtained by [52]

$$p_{\mathrm{cum}}(\mathbf{r}) = \frac{\beta}{4\rho_0 c_0^2}\iint_V p_1(\mathbf{r}_{\mathrm{v}})p_2^*(\mathbf{r}_{\mathrm{v}})H_0^{(1)}(k|\mathbf{r}-\mathbf{r}_{\mathrm{v}}|)k^2 \mathrm{d}^2\mathbf{r}_{\mathrm{v}}, \tag{2}$$

where V represents the entire space to be integrated, $H_0^{(1)}(\cdot)$ is the first-kind Hankel function of order zero, and k is the wave number of the DFW. The local component, on the other hand, is obtained according to the Lagrangian density as [53]

$$p_{\mathrm{loc}}(\mathbf{r}) = \left(\frac{\omega_1}{\omega_2} + \frac{\omega_2}{\omega_1} - 1\right)\frac{p_1(\mathbf{r})p_2^*(\mathbf{r})}{2\rho_0 c_0^2} - \frac{\rho_0}{2}\mathbf{v}_1(\mathbf{r})\cdot\mathbf{v}_2^*(\mathbf{r}), \tag{3}$$

where $\omega_i = 2\pi f_i$, $\mathbf{v}_i(\mathbf{r})$ is the particle velocity of ultrasound at the frequency of f_i, and $i = 1, 2$.

Several points can be noted upon inspecting Eqs. (2) and (3). When the two ultrasound beams are orthogonal, as illustrated in Fig. 1, the product $p_1(\mathbf{r})p_2^*(\mathbf{r})$ is negligible except in the area where the two beams intersect. Therefore, the cumulative nonlinear effect is weak as it is determined by the integration of $p_1(\mathbf{r})p_2^*(\mathbf{r})$ over the entire space as shown by Eq. (2). On the other hand, the local nonlinear effect given by Eq. (3) is dictated by the local ultrasound field (without integration) and is significant at the two focal points where the two beams meet. More importantly, Eq. (3) suggests that the DFW pressure field due to the local nonlinear effect is directly related to the pressure fields p_i, which carry information and resolution at the carrier frequencies f_i. Assuming that the difference frequency is considerably lower than the carrier frequencies, it then becomes possible to achieve deep subdiffraction

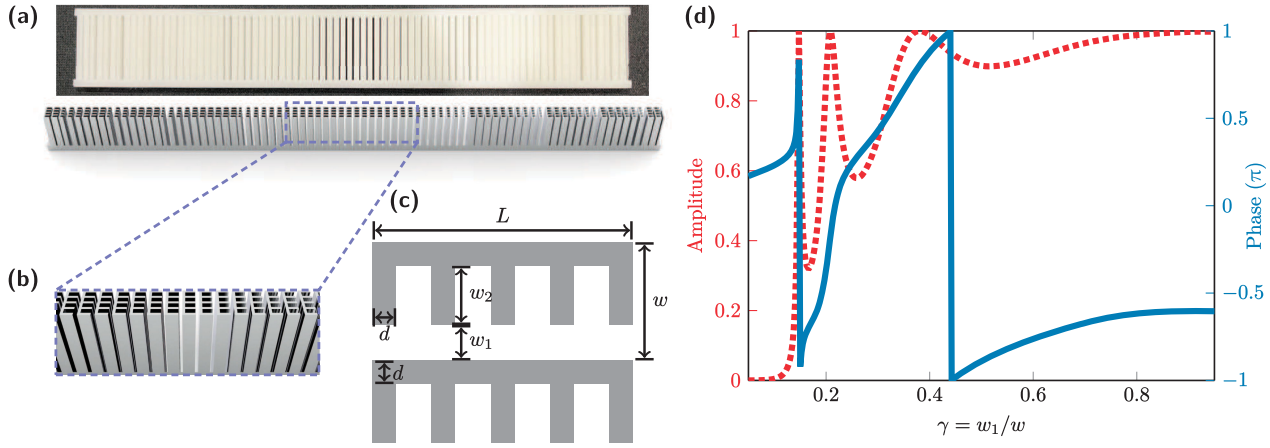

FIG. 2. Phase masks for beam focusing. (a) The photo and cut view of the metasurface-enabled phase mask consisting of 80 units. (b) A close-up view of the phase mask. (c) Top view of two unit cells of the phase mask where the adjustable geometrical parameters are marked. (d) The amplitude (dashed line) and phase (solid line) of the transmission coefficient of the unit cell as a function of the scale factor γ.

focusing at the difference frequency using the local nonlinear effect. It should be pointed out that when the two ultrasound beams are collinear, they form a system known as the "parametric array" [37,54]. In this configuration, the product $p_1(\mathbf{r})p_2^*(\mathbf{r})$ is non-negligible over the space to be integrated. On the other hand, the local nonlinear effect is largely mitigated due to the relation $p_1 p_2^* \approx \rho_0^2 c_0^2 v_1 v_2^*$ for quasiplane waves. This leads to a more pronounced cumulative nonlinear effect that overshadows the mitigated local nonlinear effect, leading to blurred images. This is the key reason why subwavelength focusing has not been achieved using parametric arrays. For more information on the focusing performance using the parametric array, the readers are referred to Sec. 6 of Supplemental Material [45].

Design of the phase mask for focusing.—As shown in Fig. 2(a)–2(c), we propose a metasurface-based phase mask for precise phase control of sound and beam focusing. The phase mask is constructed using comblike subwavelength unit cells consisting of a long slit and four side-loaded short slits. This is a modified structure from a previously reported metasurface unit cell based on side-loaded Helmholtz resonators [55] for better 3D printability at ultrasound frequency range. The short slits in the comblike structure are connected in series to provide the desired acoustic reactance to tune the phase of the incident wave. The designed frequency of the phase mask is set as $f_u = 25$ kHz, but has a bandwidth covering the two carrier frequencies $f_1 = f_u + f/2$ and $f_2 = f_u - f/2$, as shown in Sec. 3 of the Supplemental Material [45]. Here, f denotes the frequency of the DFW. The wavelength at f_u is $\lambda_u = 13.72$ mm. The width of the unit cell is $w = \lambda_u/3.5 = 3.92$ mm. The length of the unit cell, L, is $0.6\lambda_u$. Each phase mask has a total length of 313.6 mm consisting of $N = 80$ elements. The thickness of the wall is $d = \lambda_u/21$. The scale factor γ is defined as w_1/w, where w_1 is a geometrical parameter marked in Fig. 2(c). As shown in Fig. 2(d), a full coverage of phase shift from $-\pi$ to π can be achieved by varying γ.

The scale factor γ of each unit cell of the two phase masks is deigned to achieve a desired phase modulation on the incident ultrasonic waves [1]. The first phase mask is designed to focus the ultrasound at a distance of 200 mm, and the corresponding wave field simulated by COMSOL Multiphysics at 24.75 kHz is shown in Fig. 3(a). The second phase mask is designed to focus the ultrasound at two focal points located 200 mm away from the source separated approximately by 50 mm. The corresponding simulated wave field at 25.25 kHz is displayed in Fig. 3(b). The scale factor and the transmitted phase and amplitude of each unit cell can be found in Sec. 2 of the Supplemental Material [45]. In the simulation, the on-surface vibration velocity of the source is set as $v_0 = 0.2$ m/s, i.e., a on-surface sound pressure level of 129 dB. The wave fields obtained by COMSOL are then used to calculate the DFW fields using MATLAB according to Eqs. (1)–(3), where the integrals are numerically computed using Gauss-Legendre quadrature.

Figure 3(c) shows the numerical results of the DFW pressure field at the difference-frequency of 500 Hz (λ is 686 mm), resulted from the carrier sound fields shown in Figs. 3(a) and 3(b). Figure 3(d) presents the corresponding DFW pressure field along the line $y = 0$ with either only the local nonlinear effect or the cumulative nonlinear effect. The local effect is shown to dominate in this case while the cumulative effect is almost negligible and yields a smooth profile without any subwavelength characteristics. When considering the local effect only (which is equivalent to the total sound field due to the extremely weak cumulative effect), two pressure peaks occur at $(-23\text{ mm}, 0)$ and (25 mm, 0), which indicates that the two focal points are well resolved with a spatial resolution of 48 mm, corresponding to approximately $\lambda/14$. The full width at half

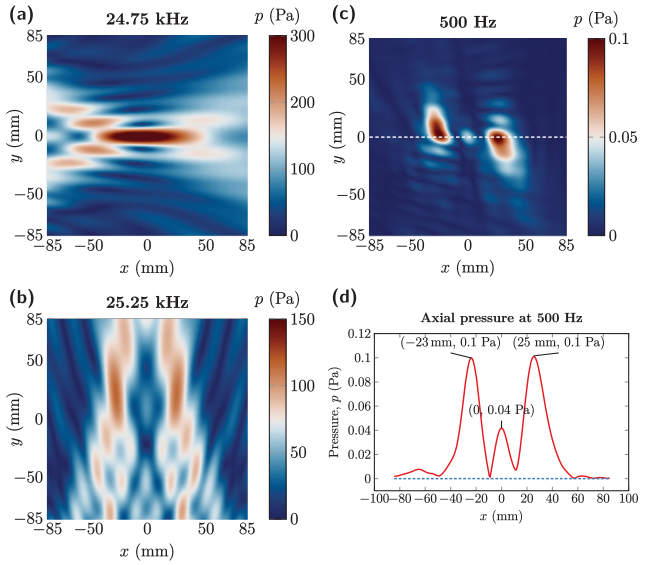

FIG. 3. The 2D pressure distributions calculated by COMSOL at 24.75 and 25.25 kHz, respectively, for (a) a one-focal-point ultrasound field generated by phase mask placed on the left and (b) a two-focal-point ultrasound field generated by a phase mask placed on the bottom. (c) The 2D pressure distribution of the DFW calculated by MATLAB using Eqs. (1)–(3) at 500 Hz, resulted from the local nonlinear interaction of waves at the two carrier frequencies. (d) The pressure field distributions along the line $y = 0$ shown as the dashed line in Fig. 3(c). Solid line, the solution with only the local nonlinear effect; dashed line, the solution with only the cumulative nonlinear effect.

maximum (FWHM) of the two individual peaks at $x = -23$ mm and $x = 25$ mm are 15 mm ($\lambda/45.7$) and 18 mm ($\lambda/38.1$), respectively, while a secondary peak is present at the center with an amplitude less than half of the maximal pressure. This undesired peak is due to the secondary peak shown in Fig. 3(b) at the origin (0,0). This is due to the limitation of the phase mask employed in this Letter, which only allows adjustments to the phase. This undesired peak could potentially be eliminated if we had the capability to tune both the amplitude and phase of the ultrasound source (see Sec. 5 in Supplemental Material for details [45]). It is interesting to observe that, not only the two focal points are resolved at a deep subdiffraction resolution, they are also both located beyond the Rayleigh distance $\pi a^2/\lambda$ of the DFW, which demonstrates the important feature of this approach for far-field subdiffraction control of sound. Though the Rayleigh distance is normally defined for a circular source in 3D space, the far field of a line source in 2D space also occurs for distances greater than the Rayleigh distance [56]. For comparison, the performance of linear acoustic focusing with the same configuration is presented in Sec. 4 of the Supplemental Material [45].

Experimental validations.—Figure 4 displays the experimental setup and results. The 2D sound field is measured between two acrylic plates with a separation of 3 cm. A Cartesian coordinate system Oxy is established with its origin at the center of the measurement region, as shown in Fig. 4(a). The measurement region is a square with dimensions of 17 cm × 17 cm. Sound pressure is measured using a 1/8-inch microphone (Brüel & Kjær Type 4138, with a dynamic range up to 168 dB). The ultrasound is

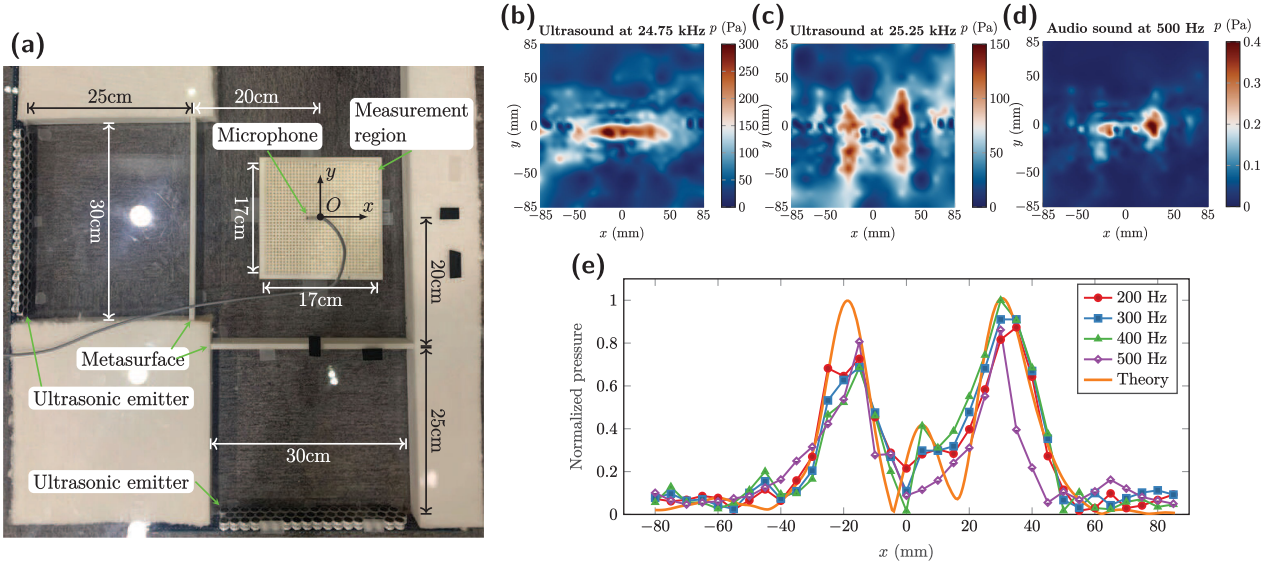

FIG. 4. (a) Photo of the experimental setup. (b) The 2D pressure distribution for a single focal point at 24.75 kHz generated by a phase mask on the left. (c) The 2D pressure distribution for two focal points at 25.25 kHz generated by a phase mask on the bottom. (d) The 2D pressure distribution of the two focal points at 500 Hz, resulting from the local nonlinear interaction between ultrasound (b) and (c). (e) Pressure distribution along the line $y = -10$ mm at 200, 300, 400, and 500 Hz. The solid line labeled "Theory" is obtained by the curve presented in Fig. 3(d).

emitted by two ultrasound arrays each consisting of 53 elements (the resonant frequency is 25 kHz; Manorshi MSO-A1625H12T) vibrating in phase. Two phase masks are 3D printed according to the design described above and are placed at a distance of 25 cm in front of the sources. The distance between the phase mask and the centroid of the measurement region is 20 cm.

Figures 4(b) and 4(c) depict the 2D ultrasound fields at 24.75 and 25.25 kHz, respectively, which are generated by the left and bottom ultrasound sources separately. The measured focusing ultrasound fields are in good agreement with those shown in the simulation, as depicted in Figs. 3(a) and 3(b). Figure 4(d) illustrates the audio sound wave at 500 Hz, showing two focal points as a result of the local nonlinear interaction of the two carrier frequency ultrasound presented in Figs. 4(b) and 4(c). The audio sound pressure along the line $y = -10$ mm is shown in Fig. 4(e), and it can be observed that two pressure peaks occur at -15 and 30 mm. A deep subdiffraction resolution of 45 mm ($\lambda/15$) is achieved at a distance of 1.8 times the Rayleigh distance (112.6 mm) for this case.

To investigate the performance of the system at different frequencies, we measured the audio sound along the line $y = -10$ mm for difference-frequency f ranging from 200 to 500 Hz with increments of 100 Hz, and the measured results are presented in Fig. 4(e). We did not include results for the difference-frequency being lower than 200 Hz due to the low signal-noise ratio and the strong spurious sound effect at low frequencies [57]. Two pressure peaks can be consistently observed with a same separation of approximately 45 mm, while the FWHM of each peak slightly increases at lower frequencies. The measured results demonstrate that the subwavelength focusing is effective over a broad bandwidth at low frequencies (more than 1 octave band in experiments). It is worth highlighting that the proposed local-nonlinearity-based technique remains applicable even at higher DFW frequencies, as evidenced by the simulation results showcased in Sec. 5 of the Supplemental Material [45]. The wavelength at 200 Hz is 1.715 m, and the corresponding Rayleigh distance, with a source dimension of $a = 156.8$ mm in experiments, is 45 mm. The measured results suggest that the system achieves a deep subdiffraction resolution of up to $\lambda/38$ (at 200 Hz) in the far field with a distance of 200 mm, which is 4.4 times the Rayleigh distance (45 mm).

Conclusion.—In summary, we present here the theoretical, numerical, and experimental evidence of deep subdiffraction acoustic focusing using the local nonlinear effect. Such an unusual wave behavior can be attributed to the fact that the DFW inherits the diffraction characteristics of the carrier frequencies which are significantly higher, and therefore rendering details at much smaller spatial resolution. This Letter, therefore, opens the door to subdiffraction control of sound using nonlinear acoustics and can be readily extended to 3D wave field patterning and high-resolution volumetric holograms [58–60] beyond beam focusing. This concept becomes particularly intriguing when considering the primary waves at ultrasound frequencies while the DFW operates within the audible frequency range, as the proposed method would have significant implications for high-resolution multizone sound field reproduction.

This work was supported by the National Key R&D Program of China (Grants No. 2022YFA1404402 and No. 2017YFA0303700), the National Natural Science Foundation of China (Grants No. 12274221, No. 11634006, and No. 12174190), High-Performance Computing Center of Collaborative Innovation Center of Advanced Microstructures, the Priority Academic Program Development of Jiangsu Higher Education Institutions, and the Penn State Startup funds for Dr. Yun Jing.

*These authors contributed equally to this work.
†liangbin@nju.edu.cn
‡jing.yun@psu.edu
§jccheng@nju.edu.cn

[1] K. Melde, A. G. Mark, T. Qiu, and P. Fischer, Nature (London) **537**, 518 (2016).
[2] E. G. Williams, *Fourier Acoustics: Sound Radiation and Nearfield Acoustical Holography* (Academic, San Diego, CA, 1999).
[3] E. G. Williams and J. D. Maynard, Phys. Rev. Lett. **45**, 554 (1980).
[4] J. Li and C. T. Chan, Phys. Rev. E **70**, 055602(R) (2004).
[5] S. Guenneau, A. Movchan, G. Pétursson, and S. A. Ramakrishna, New J. Phys. **9**, 399 (2007).
[6] G. Ma and P. Sheng, Sci. Adv. **2**, e1501595 (2016).
[7] C. Errico, J. Pierre, S. Pezet, Y. Desailly, Z. Lenkei, O. Couture, and M. Tanter, Nature (London) **527**, 499 (2015).
[8] P. Packo and D. Torrent, Phys. Rev. Appl. **17**, 064040 (2022).
[9] C. Hu, J. Weng, Y. Ding, B. Liang, J. Yang, and J. Cheng, Appl. Phys. Lett. **118**, 203504 (2021).
[10] Y. N. Makov, V. J. Sánchez-Morcillo, F. Camarena, and V. Espinosa, Ultrasonics **48**, 678 (2008).
[11] R. Oldfield and I. Drumm, in *Audio Engineering Society Convention 137* (Audio Engineering Society, New York, 2014), pp. 1–10.
[12] Z. J. Wong, Y. Wang, K. O'Brien, J. Rho, X. Yin, S. Zhang, N. Fang, T.-J. Yen, and X. Zhang, J. Opt. **19**, 084007 (2017).
[13] A. Poddubny, I. Iorsh, P. Belov, and Y. Kivshar, Nat. Photonics **7**, 948 (2013).
[14] S. A. Cummer, J. Christensen, and A. Alù, Nat. Rev. Mater. **1**, 1 (2016).
[15] Z. Liu, X. Zhang, Y. Mao, Y. Y. Zhu, Z. Yang, C. T. Chan, and P. Sheng, Science **289**, 1734 (2000).
[16] X. Chen, Y. Luo, J. Zhang, K. Jiang, J. B. Pendry, and S. Zhang, Nat. Commun. **2**, 176 (2011).
[17] L. Zigoneanu, B.-I. Popa, and S. A. Cummer, Nat. Mater. **13**, 352 (2014).

[18] X. Zhu, B. Liang, W. Kan, X. Zou, and J. Cheng, Phys. Rev. Lett. **106**, 014301 (2011).
[19] X. Zhang and Z. Liu, Nat. Mater. **7**, 435 (2008).
[20] J. B. Pendry, Phys. Rev. Lett. **85**, 3966 (2000).
[21] N. Fang, H. Lee, C. Sun, and X. Zhang, Science **308**, 534 (2005).
[22] Y. Xiong, Z. Liu, C. Sun, and X. Zhang, Nano Lett. **7**, 3360 (2007).
[23] S. Durant, Z. Liu, J. M. Steele, and X. Zhang, J. Opt. Soc. Am. B **23**, 2383 (2006).
[24] Z. Liu, S. Durant, H. Lee, Y. Pikus, N. Fang, Y. Xiong, C. Sun, and X. Zhang, Nano Lett. **7**, 403 (2007).
[25] C. Ma, S. Kim, and N. X. Fang, Nat. Commun. **10**, 204 (2019).
[26] J. Li, L. Fok, X. Yin, G. Bartal, and X. Zhang, Nat. Mater. **8**, 931 (2009).
[27] J. Sun, M. I. Shalaev, and N. M. Litchinitser, Nat. Commun. **6**, 7201 (2015).
[28] Z. Liu, H. Lee, Y. Xiong, C. Sun, and X. Zhang, Science **315**, 1686 (2007).
[29] C. Shen, Y. Xie, N. Sui, W. Wang, S. A. Cummer, and Y. Jing, Phys. Rev. Lett. **115**, 254301 (2015).
[30] J. Zhu, J. Christensen, J. Jung, L. Martin-Moreno, X. Yin, L. Fok, X. Zhang, and F. J. Garcia-Vidal, Nat. Phys. **7**, 52 (2011).
[31] Y.-X. Shen, Y.-G. Peng, F. Cai, K. Huang, D.-G. Zhao, C.-W. Qiu, H. Zheng, and X.-F. Zhu, Nat. Commun. **10**, 3411 (2019).
[32] F. M. Huang, Y. Chen, F. J. G. de Abajo, and N. I. Zheludev, J. Opt. A **9**, S285 (2007).
[33] G. Ma, X. Fan, F. Ma, J. de Rosny, P. Sheng, and M. Fink, Nat. Phys. **14**, 608 (2018).
[34] B. Orazbayev and R. Fleury, Phys. Rev. X **10**, 031029 (2020).
[35] V. Yu. Zaitsev, A. Sutin, I. Yu. Belyaeva, and V. Nazarov, J. Vib. Control **1**, 335 (1995).
[36] G. ter Haar and C. Coussios, International Journal of Hyperthermia **23**, 89 (2007).
[37] W.-S. Gan, J. Yang, and T. Kamakura, Appl. Acoust. **73**, 1211 (2012).
[38] A. Marzo, S. A. Seah, B. W. Drinkwater, D. R. Sahoo, B. Long, and S. Subramanian, Nat. Commun. **6**, 8661 (2015).
[39] T. Hoshi, M. Takahashi, T. Iwamoto, and H. Shinoda, IEEE Trans. Haptics **3**, 155 (2010).
[40] S. I. Aanonsen, T. Barkve, J. N. Tjøtta, and S. Tjøtta, J. Acoust. Soc. Am. **75**, 749 (1984).
[41] M. F. Hamilton and D. T. Blackstock, *Nonlinear Acoustics* (Acoustical Society of America, New York, 2008).
[42] Q. Ma, D. Zhang, X. Gong, and Y. Ma, J. Acoust. Soc. Am. **119**, 2518 (2006).
[43] N. D. Londhe and J. S. Suri, Journal of medical systems **40**, 279 (2016).
[44] M. Červenka and M. Bednařík, J. Acoust. Soc. Am. **146**, 2163 (2019).
[45] See Supplemental Material at http://link.aps.org/supplemental/10.1103/PhysRevLett.131.234001 for the extended second-order nonlinear wave equation, parameters, and performance of the designed phase masks, performance of linear and nonlinear acoustic focusing, which includes Refs. [46–50].
[46] B. Hamilton and S. Bilbao, JASA Exp. Lett. **1**, 092401 (2021).
[47] A. D. Pierce, *Acoustics: An Introduction to Its Physical Principles and Applications*, 3rd ed. (Springer Nature, Cham, Switzerland, 2019).
[48] K. G. Foote, J. Acoust. Soc. Am. **150**, R1 (2021).
[49] J.-W. Choi and Y.-H. Kim, J. Acoust. Soc. Am. **111**, 1695 (2002).
[50] J.-H. Chang, C.-H. Lee, J.-Y. Park, and Y.-H. Kim, J. Acoust. Soc. Am. **125**, 2091 (2009).
[51] J. Zhong, R. Kirby, and X. Qiu, J. Acoust. Soc. Am. **149**, 1524 (2021).
[52] J. Zhong, R. Kirby, M. Karimi, and H. Zou, J. Acoust. Soc. Am. **150**, 3797 (2021).
[53] M. Červenka and M. Bednařík, J. Acoust. Soc. Am. **151**, 4046 (2022).
[54] P. J. Westervelt, J. Acoust. Soc. Am. **35**, 535 (1963).
[55] Y. Li, X. Jiang, B. Liang, J.-C. Cheng, and L. Zhang, Phys. Rev. Appl. **4**, 024003 (2015).
[56] L. W. Schmerr Jr, *Fundamentals of Ultrasonic Phased Arrays* (Springer, New York, 2014).
[57] P. Ji, W. Hu, and J. Yang, Ultrasonics **67**, 160 (2016).
[58] T. Fushimi, A. Marzo, B. W. Drinkwater, and T. L. Hill, Appl. Phys. Lett. **115**, 064101 (2019).
[59] R. Hirayama, D. Martinez Plasencia, N. Masuda, and S. Subramanian, Nature (London) **575**, 320 (2019).
[60] K. Hasegawa, H. Shinoda, and T. Nara, J. Appl. Phys. **127**, 244904 (2020).